Hyperbolic Metamaterial Devices for Wavefront Manipulation

Xiang Yin, Hua Zhu, Huijie Guo, Ming Deng, Tao Xu, Zhijie Gong, Xun Li, Zhi Hong Hang, Chao Wu, Hongqiang Li, Shuqi Chen, Lei Zhou,* and Lin Chen*

Metasurfaces have shown great potential to reshape the wavefront of electromagnetic (EM) waves, but transmissive meta-devices face challenges of low-efficiency and/or fabrication complexities. Here, an alternative approach to realize high-efficiency transmission-mode meta-devices to control EM wavefronts, based on hyperbolic metamaterial (HMM) waveguides supporting tailored spoof surface plasmons (SSPs) on their side walls, is proposed. By manipulating the dispersions of SSPs through adjusting the HMM geometrical parameters, the phases of EM waves passing through such waveguides, which enables the design of meta-devices with desired transmission-phase profiles for particular wave-manipulation applications, can be controlled. Microwave experiments are implemented to demonstrate two wave-control effects based on the mechanism, that is, beam-deflection and focusing, and a maximum conversion efficiency of 42.9% is achieved for the anomalous refracted beam. By scaling down the HMM meta-devices, the proposal herein is applicable to optical frequencies and in principle promises significantly raised conversion efficiencies. The scheme herein can offer a higher effective refractive index and more tunable dispersion without using high-index dielectric materials, and thus can serve as an effective and robust approach to make high-efficiency transmissive meta-devices with diversified functionalities.

1. Introduction

Manipulating electromagnetic (EM) waves with controllable amplitude, phase, and polarization is always the theme in photonics research.[1–3] Metamaterials have provided an unprecedented approach to the extreme control of EM waves, leading to a variety of intriguing phenomena and applications that are unattainable with natural materials such as negative refraction,[4] super-resolution imaging,[5] and invisibility cloaking.[6] As the 2D equivalent of metamaterials, metasurfaces have shown great promises to control EM waves by locally modulating the phase, amplitude and/or polarization of the scattered field.[7–13] Distinct from traditional photonic devices (e.g., lenses) that rely on propagation phases accumulated inside the device to shape the wavefront, metasurfaces utilize the interfacial phase discontinuities introduced by subwavelength-sized planar resonators to locally control the amplitude and phase of scattered waves and thus to reshape the wavefront of EM waves. Many fascinating wave-manipulation effects were discovered based on metasurfaces, such as light bending,[7,11,13] unidirectional surface plasmon coupling,[8,14] invisibility cloaks,[6,15] flat lenses,[9,16] holography,[17,18] and generation of vortex beam.[7,19]

Transmissive metasurfaces are particularly useful in practice, but the working efficiencies of single-layer plasmonic metasurfaces are typically low. For example, a single-layer Pancharatnam–Berry (PB) metasurface, working for circularly polarized (CP) light, cannot exhibit an efficiency higher than 25%, due to

X. Yin, H. Zhu, M. Deng, Prof. X. Li, Dr. L. Chen
Wuhan National Laboratory for Optoelectronics
Huazhong University of Science and Technology
Wuhan 430074, China
E-mail: chen.lin@mail.hust.edu.cn

H. Guo, Prof. L. Zhou
State Key Laboratory of Surface Physics and Key Laboratory of Micro and Nano Photonic Structures (Ministry of Education)
Fudan University
Shanghai 200433, China
E-mail: phzhou@fudan.edu.cn

T. Xu, Prof. Z. H. Hang
College of Physics
Optoelectronics and Energy and Collaborative Innovation Center of Suzhou Nano Science and Technology
Soochow University
Suzhou 215006, China

Z. Gong, C. Wu, Prof. H. Li
School of Physics Science and Engineering
Shanghai Key Laboratory of Special Artificial Microstructure Materials and Technology
Tongji University
Shanghai 200092, China

Prof. S. Chen
The MOE Key Laboratory of Weak Light Nonlinear Photonics
School of Physics and TEDA Institute of Applied Physics
Nankai University
Tianjin 300071, China

lacking of magnetic responses to match the impedance.[20,21] To build metasurfaces working for linearly polarized (LP) light, one needs to choose a collection of meta-atoms with transmission phases covering the full 2π range. However, a single plasmonic resonator, no matter electric or magnetic, can only shift the phase of EM wave in the range of π. To overcome these issues, Huygens' surfaces[21–23] and multilayer cascaded metasurfaces[20] were proposed which can exhibit significantly enhanced working efficiencies for the transmission mode. More recently, dielectric metasurfaces were widely studied since they can further enhance the working efficiency by eliminating the ohmic losses in plasmonic systems.[11,13,19,23] However, to construct dielectric metasurfaces that offer high tranmission as well as full 2π phase coverage, the used dielectric material should have high effective index and also should be transparent in the frequency range of interest.[11,24–28] It would be of great significance if an alternative approach is proposed to make high-efficiency transmissive metasurfaces which can relax the stringent demanding for high-index materials.

In this paper, we establish an alternative approach to construct transmissive metasurfaces with high working efficiencies and broad working bands. Distinct from conventional approaches based on dielectric and plasmonic metasurfaces, our scheme requires neither high-index materials nor plasmonic resonances. We have noted in previous studies, the high effective refractive index in the hyperbolic metamaterial (HMM) waveguide has been successfully exploited to enable artificial high refractive index metamaterials,[29] indefinite optical cavities,[30] strong enhancement of spontaneous emission,[31] negative refraction,[32] superlensing effects,[33] wideband photon harvesting/absorbing,[34] and photonics hypercrystals (PHC).[35–37] Here we show that artificial waveguides with side walls being HMM can support a branch of waveguide mode, whose dispersion is fully controlled by spoof surface plasmons (SSPs) on the HMM surface,[29,30,38–43] so that the phase and amplitude of EM wave transmitted through such a waveguide can be freely modulated by adjusting the microstructures of the HMM. We note a series of studies on using HMM to further construct PHC, where high k modes are extensively employed, leading to various unique features such as enhancing light–matter interaction[35,36] and guiding surface waves at the dielectric–PHC interface with enhanced propagation distance and wave number.[37] Different from the reported PHCs, the SSP mode here does not originate from the high k modes in the HMM, and its propagation direction is normal to the metal–dielectric multilayer, rather than parallel to the metal surface. We can thus use such waveguides as a building block (meta-atom) to construct transmissive metasurfaces with desired functionalities by tailoring the phases of locally transmitted waves through adjusting the HMM structures. As an illustration of our general concept, we design and fabricate two functional devices and then perform microwave experiments to demonstrate their beam-bending or beam-focusing functionalities for LP and CP EM waves, respectively, where the experimental results are in excellent agreement with the numerical simulations. By scaling down the HMM meta-devices, our proposal can be extended to operate at optical frequencies and in principle promises significantly raised conversion efficiencies, being comparable to those with dielectric high-aspect-ratio metasurfaces recently reported. Benifiting from the great flexibility to tune the SSP modes by adjusting the structural parameters, the

HMM meta-devices exhibit the advantages of higher effective refractive indices and more tunable disperison, compared with dielectric metasurfaces.[11,25,27] The largest aspect ratios for the designed HMM meta-devices are 5.8 in the microwave range and 6.2 in the near infrared range, which is comparable to that of dieletric metasurfaces.[27,44] Since our scheme do not require any high-index materials, it thus represents an effective and robust approach to build high-efficiency wavefront-control transmissive meta-devices, at frequencies where appropriate high-index materials are difficult to find. We have noted in a recent study that the authors have used rigorous treatment of the wave equation, instead of the ray-optics approximations, to outline the theoretical limitations on working efficiency of passive gradient metasurfaces for wave manipulations, especially for large-angle wave bending applications.[45] They have further shown that, conventional ray-optics approximations are insufficient to design metasurfaces for such extreme wave manipulations, and the required impedance profile needs to include both lossy and gain media in general to guarantee 100% efficiency even under extreme conditions. Since our metasurfaces are not for very large bending angles, the issue pointed out in ref.45 is not that severe, and thus we still used the conventional Huygens' principle to perform the designs.

2. Results

2.1. Operating Principle

A typical HMM waveguide comprised of alternating metal–dielectric multilayer of finite width, W, surrounded with air is shown in **Figure 1**a. We are interested in searching for the surface bounded EM waves, that is, SSPs, at both sides of the HMM-air interfaces and calculating the dispersion curve (frequency f vs propagation constant k_z along the z-direction). In the microwave and terahertz domain, the metal can be treated as perfect electric conductor. By using a modal expansion method to write out the components of the EM fields in each region and then combining the boundary conditions that E_z and H_y are continuous at the HMM–air interfaces, the dispersion relations of the surface bounded waves can be expressed as (see Note 1A, Supporting Information, for more details regarding the derivation process)

$$\begin{cases} \sqrt{k_z^2 - k_0^2} = -k_0 S_0^2 \cot(n_d k_0 W/2)/n_d, & \text{odd modes} \\ \sqrt{k_z^2 - k_0^2} = k_0 S_0^2 \tan(n_d k_0 W/2)/n_d, & \text{even modes} \end{cases} \tag{1}$$

where k_0 is the wavenumber in free space, t_d and P_z represent the thicknesses of dielectric layers and the lattice constant along the z-direction, respectively, n_d denotes the refractive index of the dielectric layers, and $S_0 = \sqrt{\frac{t_d}{P_z} \frac{\sin(k_z t_d/2)}{k_z t_d/2}}$. The dispersion relations represented by Equation (1) indicate that the HMM waveguide supports the propagation of plasmon-like modes with the asymptotes being controlled mainly by W and n_d. Figure 1b illustrates that both the dispersion curves for the symmetric and asymmetric SSP modes deviate significantly from the light line (black dashed line). The theoretical results are well consistent with those numerically simulated with an eigenmode solver by a
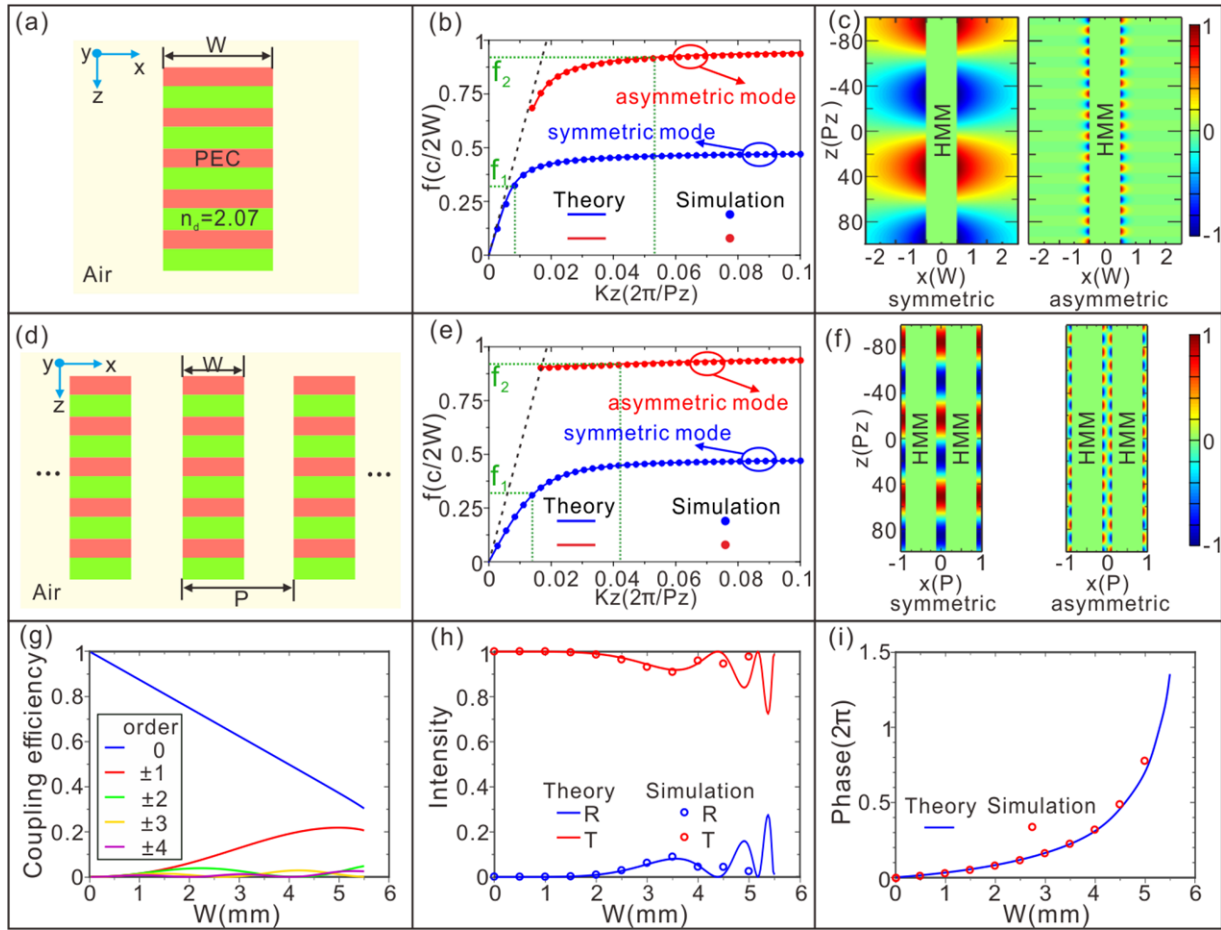
ADVANCED
SCIENCE NEWS
www.advancedsciencenews.com

LASER
&PHOTONICS
REVIEWS

www.lpr-journal.org

Figure 1. Schematic diagram of 1D-HMM waveguide (array) and dispersion curves. a) 1D-HMM waveguide comprised of alternating metal–dielectric multilayer of finite width, W, surrounded with air. The thicknesses of metal and dielectric layers are represented by t_m and t_d, respectively, and the lattice constant along the z-direction is denoted as P_z $(= t_m + t_d)$. The refractive index of the dielectric layer is assumed to be $n_d = 2.07$. b) Dispersion curves calculated for $t_m = 0.04$ mm, $t_d = 0.2$ mm, and $W = 6$ mm. c) Distributions of the real part of E_x of symmetric and asymmetric SSP modes for the 1D-HMM waveguide at $f_1 = 0.32c/2W$ and $f_2 = 0.92c/2W$, respectively. d) 1D-HMM waveguide array with the lattice constant along the x-direction is represented by P. e) Dispersion curves calculated for $t_m = 0.04$ mm, $t_d = 0.2$ mm, $W = 6$ mm, and $P = 8$ mm. f) Distributions of the real part of E_x of symmetric and asymmetric SSP modes for the 1D-HMM waveguide array at $f_1 = 0.32c/2W$ and $f_2 = 0.92c/2W$, respectively. g) Dependence of the coupling efficiency between the n-order ($n = 0, \pm 1, \pm 2, \ldots$) diffraction waves and the guided zero-order eigen mode of the 1D-HMM waveguide array on W at 12 GHz. h) Theoretical and simulated reflectance and transmittance and i) phase shift versus W at 12 GHz. All the other geometrical parameters are the same as those in Figure 2. In this work, all the simulations except the dispersion calculations are conducted by the Lumerical FDTD Solution.

commercial Bandsolve software.[46] In contrast to a conventional SSP waveguide made by periodic indentation on a flat metallic surface,[42,43] the HMM waveguide here provides the extra dimension of the tunability of SSP dispersion relation by selecting dielectric material. The electric field diagrams of theoretical calculation in Figure 1c confirm the presence of the SSP modes, which are highly confined at a rather deep subwavelength scale at both sides of HMM–air interfaces. To periodically arrange the HMM waveguides in an array shown in Figure 1d, the SSP modes in adjacent units will interact with each other due to the overlap of their evanescent fields. Therefore, the modal characteristics of the SSP modes could be significantly influenced by the coupling strength, depending on the gap separations between the adjacent HMM waveguides. Using the same calculation approach described above, the dispersion relation for an HMM waveguide

array can be expressed as (see Note 1B, Supporting Information, for the derivation process)

$$
\begin{cases}
\sqrt{k_z^2 - k_0^2} = -k_0 S_0^2 \dfrac{1 - e^{-\sqrt{k_z^2 - k_0^2}g}}{1 + e^{-\sqrt{k_z^2 - k_0^2}g}} \cot(n_d k_0 W/2)/n_d, & \text{odd modes} \\[4mm]
\sqrt{k_z^2 - k_0^2} = k_0 S_0^2 \dfrac{1 + e^{-\sqrt{k_z^2 - k_0^2}g}}{1 - e^{-\sqrt{k_z^2 - k_0^2}g}} \tan(n_d k_0 W/2)/n_d, & \text{even modes}
\end{cases}
$$

(2)

in which g is the gap separation between the adjacent HMM waveguides and P $(= g + W)$ represents the lattice constant along the x-direction. The calculated dispersion curves (Figure 1e) and electric field diagrams (Figure 1f) notably reflect the

coupling effect of the SSP modes between the adjacent HMM waveguides. The effective refractive index, k_z/k_0, of the symmetrical SSP mode at $f_1 = 0.32c/2W$ is increased from 1.21 for the single waveguide (Figure 1b) to 2.7 for the waveguide array with the gap separation of $0.25P$ (Figure 1e). In addition to tuning the geometrical parameters of the HMM waveguide, a higher effective refractive index of the SSP mode could be achieved by using a smaller gap separation to enhance the coupling between the adjacent SSP modes. It should be noted here, despite the great capability of the asymmetrical SSP mode in tuning the dispersion relation, it is not suitable for the design of functional devices due to zero coupling with the incident waves. This is because that, the filed distributions of the aysmmetric SSP mode and the incident EM waves is an odd and even functions, respectively, hence their field overlap is zero[47] (see Note 3, Supporting Information, for more details). Consequently, the asymmetric SSP mode can not be directly excited by the normally incident EM waves and is not applicable for the design of functional devices.

The remaining question after calculating the guided SSP modes is how to achieve the maximum transmission by controlling the coupling efficiency between the incident waves and the SSP modes. We have developed a rigorous modal theory to estimate the complex reflection/transmission coefficients for the HMM waveguide array (see Note 2, Supporting Information, for more details). The coupling efficiency between the n-order diffracted waves in the air and the m-th symmetric mode supported by the HMM waveguide array, $\eta^{(n,m)}$, contributes to the transmission efficiency (Figure 1g). In our case, merely the fundamental SSP mode ($m = 0$) should be taken into account due to the selected structural parameters for the HMM waveguide array. Due to the subwavelength spacing between the adjacent HMM waveguides the high-order diffracted waves are evanescent waves and can not reach the far-field, but their presences are crucial to make the boundary conditions at the air–HMM interface satisfied, and thus they can indirectly modify the final strength of the zero-order SSP mode. As a result, the coupling efficiency between the diffraction waves for all orders and the zero-order SSP mode should be taken into account when considering the transmission efficiency (see Note 4, Supporting Information, for more details regarding the contribution of the diffraction waves for all orders to the transmission efficiency). For a small value of W, the coupling efficiency between the zero-order diffraction waves and the SSP mode, $\eta^{(0,0)}$, predominantly contributes to the high transmission efficiency (nearly 100% in Figure 1h). As W increases, high-order coupling efficiency, $\eta^{(n,0)}$ ($|n| > 0$), occurs and tends to make extra contributions to the transmission efficiency. As a result, it can still keep a high level of transmission efficiency despite the fact that the contribution from zero-order coupling efficiency decreases. The proposed HMM meta-atom facilitates great flexibility in shifting the phase of EM wave within the range of 2π with a wide tuning range of W (Figure 1i), but without the sacrifice of notably reduced transmission efficiency.

Understanding the EM characteristics of an HMM waveguide array above-mentioned helps us design a transmissive wavefront manipulation device. It should be emphasized here, the phase control with the HMM waveguide array can be fulfilled over a wide range of frequencies throughout the visible, near-infrared, mid-infrared, terahertz, and microwave spectral regions by freely tuning the geometry defining the multilayer.[48,49] Here

as an example, we have chosen the microwave regime to investigate the modal dispersions for the three HMM waveguide arrays (**Figure 2**a–c) as Cu and FR4 are taken as the metal and dielectric layers. One can see from Figure 2d that there exists a significant difference of the propagation constant for different widths of the 1D-HMM waveguide (Figure 2a), apparently indicating that arbitrary phase shift could be introduced for linearly polarized EM waves by arranging varied width along the x-direction. An array of squared-shaped HMM (SHMM) waveguides (Figure 2b) offers the capability of guiding SSPs at both sides of the HMM–air interfaces along x- and y-polarization directions simultaneously, and hence could impart arbitrary phase shift for linearly polarized EM waves by varying the HMM width as well (Figure 2e). What makes the SHMM differ from the 1D-HMM is that the phase retardation offered by the former is polarization-independent, whereas that by the latter is polarization-dependent. This implies that the 1D-HMM waveguide arrays apply to the design of polarization-dependent wavefront devices, while the SHMM waveguide arrays are suitably designed for polarization-independent wavefront devices. However, a SHMM waveguide array fails to introduce phase difference for the two orthogonal polarization directions due to the equivalent SSP modes along x- and y-polarizations. An array of rectangle-shaped HMM (RHMM) waveguides (Figure 2c) can address this issue since the SSP modes are guided along the two orthogonal polarization directions with different propagation constants. Assuming the RHMM waveguide array, rotated by α with respect to x-axis, is illuminated with a beam of CP EM wave, the transmitted electric field can be written as

$$E_t = \frac{1}{2}(t_x + t_y)\vec{e}_{\mathrm{co}} + \frac{1}{2}(t_x - t_y)e^{\sigma j2\alpha}\vec{e}_{\mathrm{cross}} \qquad (3)$$

where the first term corresponds to the co-polarized EM waves, and the second term is associated with the cross-polarized EM waves that carries a PB phase, t_x (t_y) represents the complex transmission coefficient for x(y)-polarized incidence, $\vec{e}_{\mathrm{co}}$ and $\vec{e}_{\mathrm{cross}}$ are the CP-based vectors for the co- and cross-polarized EM waves, respectively, and $\sigma = \pm 1$ denotes the incident EM waves with right circular polarization (RCP), and left circular polarization (LCP), respectively. On the basis of Equation (3), a complete polarization conversion for the CP EM waves occurs as $t_x = -t_y$, which basically ensures the RHMM waveguide array serves as a half-wave plate. Meanwhile, the cross-polarized EM wave carries a PB phase, $2\sigma\alpha$, that is twice of the rotation angle. Consequently, we are able to introduce arbitrary phase distributions for the CP EM waves by arranging the RHMM waveguide array with the rotation angle successively varied along x-axis.

Figure 3 schematically illustrates the wavefront shaping structures as beam deflectors and focusing lens with the HMM waveguides. To construct a beam deflector, phase shifts covering $0–2\pi$ range are required to provide full control of the wavefront. Besides, a super cell of the HMM waveguides should be designed to enable the phase shift, $\varphi_d(x)$, and location, x, to satisfy the following equation:

$$\varphi_d(x) = \varphi_{0d} + \frac{2\pi}{L_x}x \qquad (4)$$

**ADVANCED
SCIENCE NEWS**

www.advancedsciencenews.com

LASER
& PHOTONICS
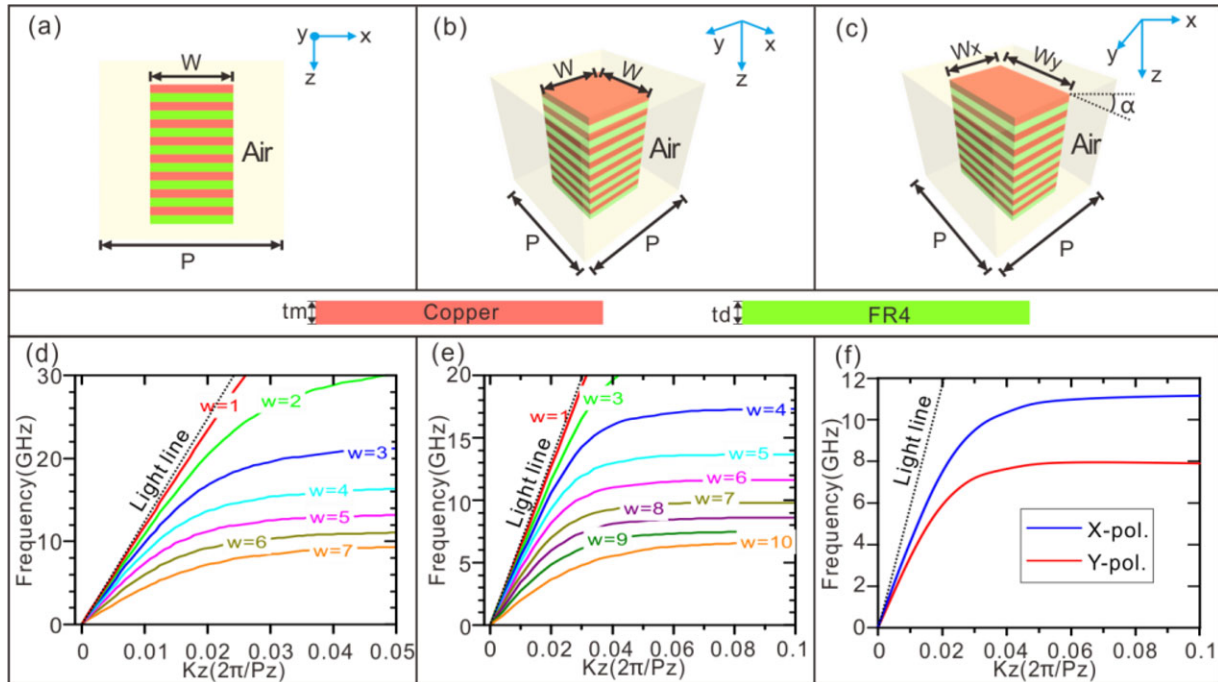REVIEWS

www.lpr-journal.org

Figure 2. Schematic diagram of three kinds of HMM waveguide arrays and dispersion curves. Side views for a) 1D-HMM waveguide array, b) square HMM (SHMM) waveguide array, and c) rectangular HMM (RHMM) waveguide array rotated by α with respect to x-axis. d) The dispersion relations for x-polarization calculated for $P = 8$ mm, $t_m = 0.04$ mm, and $t_d = 0.2$ mm with different 1D-HMM widths. e) The dispersion relations for $x(y)$-polarization calculated for $P = 11$ mm, $t_m = 0.068$ mm, and $t_d = 0.4$ mm with different SHMM widths. f) The dispersion relations for x- and y-polarizations with $P = 13$ mm, $W_x = 6$ mm, $W_y = 9$ mm, and $P_z = 0.538$ mm ($t_m = 0.068$ mm, $t_d = 0.47$ mm) for the RHMM waveguide array. Cu and FR4 are selected as the metal and dielectric layers, respectively, with the conductivity of Cu 5.8×10^7 s m^{-1}, and the relative permittivity and loss tangent of FR4 equal to 4.3, and 0.025 within the frequency range considered.

where L_x is the lattice constant of a super cell along the x-direction, and φ_{0d} is the phase shift of the first subunit in a super cell. This equation applies to the design of beam deflectors working both for linear (Figure 3a,b), and circular polarizations (Figure 3d). As for the focusing lens for linear (Figure 3c) and circular (Figure 3e) polarizations, the spatial phase distribution along the x-direction should abide by a hyperboloidal profile as

$$\varphi_f(x) = \varphi_{0f} + k_0 \left(f - \sqrt{x^2 + f^2} \right) + 2m\pi \tag{5}$$

Here, φ_{0f} is the initial phase shift at the center of the focusing lens ($x = 0$), f represents the focusing length, and m is the arbitrary integer.

2.2. Design, Fabrication, and Measurement of Beam Deflectors and Lenses

The above-mentioned concept of using HMM meta-devices for diverse control of EM wavefront can be realized in any frequency regime, owing to the great flexibility in the design of the HMM waveguide arrays over the entire spectral regime. Here we choose to design and realize beam deflectors and lenses at the microwave frequencies, and verify their performance with simulations and a proof-of-concept experiment. Choosing the working frequency for the designed structures, we have successfully designed and fabricated five samples to enable those practical functionalities

presented in Figure 3. The detailed sample fabrication can be found in Note 6, Supporting Information.

Figure 4a shows the fabricated 1D-HMM waveguide array with $L_x = 80$ mm for linearly polarization-dependent beam deflecting. The width of the individual HMM waveguide in a super cell is presented in Figure 4b, in which their phase distributions cover 0–2π with a constant step of $\pi/5$ and comply with Equation (4) (Figure 4c). It should be noted here, the width for the first HMM waveguide is set to zero so as to enable zero phase shift. In the following work, a HMM waveguide with zero width is used for the design when zero phase shift is required. Meanwhile, the transmission amplitude is kept high and almost uniform. All these conditions ensure the formation of new wavefront for an incoming x-polarized plane-wave with normal incidence (The detailed near-field scanning experiments can be retrieved to Note 6, Supporting Information, and the simulated and measured near-field electric field distributions of E_x are shown in Note 7, Supporting Information). The far-field intensity distributions from the simulation (Figure 4d) agree well with the measurement (Figure 4e), and both of them validate that nearly all the transmitted EM waves are refracted along the anomalous angle of 18.2°, predicted by general Snell's law[7] (The detailed far-field measurement and experimental setup are presented in Note 6, Supporting Information). The conversion efficiency, the ratio of the energy converted into the anomalous component to the total energy of the incident EM waves, reaches 43.5% in the measurement, agreeing well with the simulated value of 44.2%.
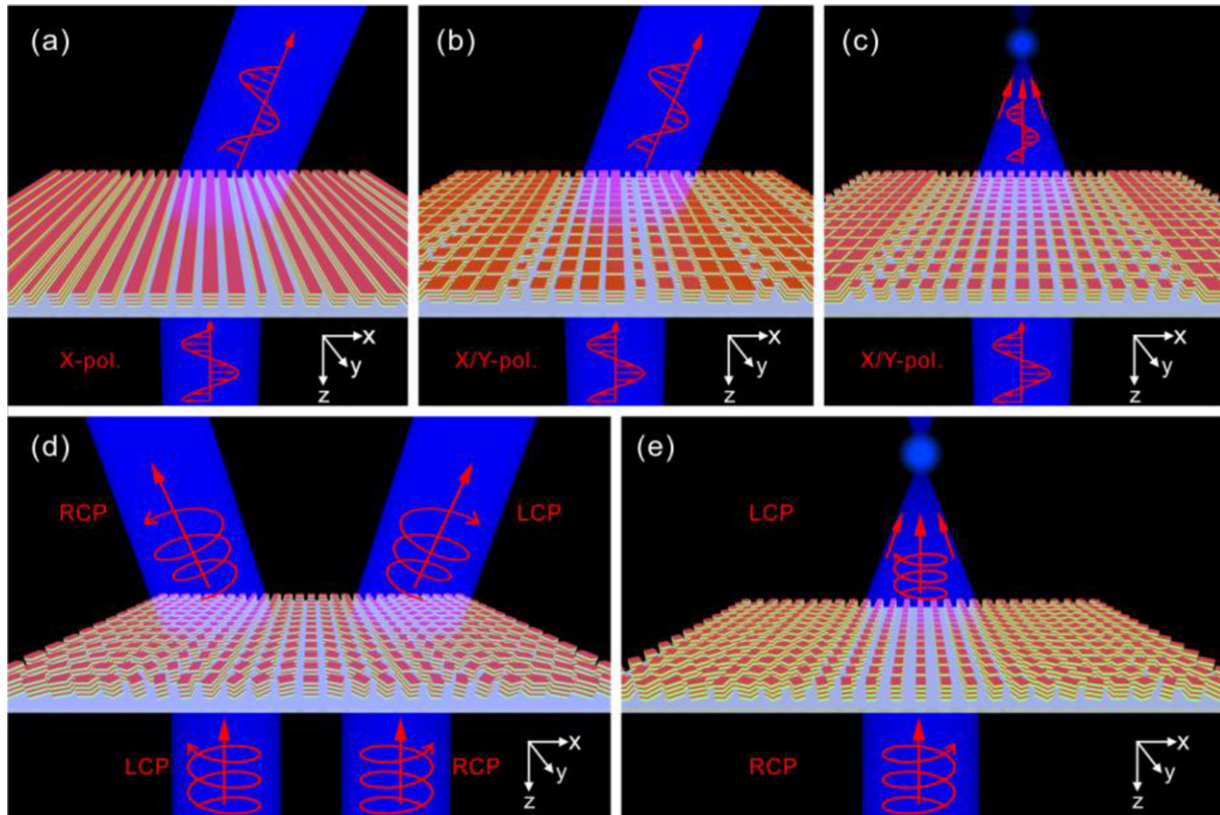
ADVANCED
SCIENCE NEWS

www.advancedsciencenews.com

LASER
&PHOTONICS
REVIEWS

www.lpr-journal.org

Figure 3. HMM waveguide arrays as beam deflectors and focusing lens. a) 1D-HMM waveguide array for polarization-dependent beam deflection. SHMM waveguide array for polarization-independent beam b) deflecting and c) focusing. RHMM waveguide array for circularly polarized beam d) deflecting and e) focusing. All the designed and fabricated samples are sited on an FR4 substrate.

Additionally, the measured diffraction efficiency, the ratio of anomalous transmitted energy to the total transmitted energy, is found as high as 82%, associated with the simulation value of 85%. It is worth noting here that no transmission is detected as the EM waves are totally reflected by the HMM waveguide array with y-polarized incidence (not shown here).

The SHMM waveguide array (Figure 4f) can be used to address the polarization-dependent issue faced by the 1D-HMM waveguide array. The detailed information for the optimization of the geometrical parameters of the SHMM waveguide array can be retrieved to Note 8, Supporting Information. Figure 4g,h present that the designed phase distributions cover full 0–2π range, and have the linear phase-gradient of $\pi/3$, required by Equation (4). Meanwhile, the high transmission amplitude by each SHMM waveguide is highly expected to deflect the EM waves along the anomalous angle with high efficiency. The far-field intensity distributions from both the simulation (Figure 4i,j) and measurement (Figure 4k,l) indicate that the anomalous angle is equivalent for x- and y-polarization incidences, and is well consistent with that retrieved by general Snell's law. The near-field electric field distributions can be referred to Note 9, Supporting Information.

By arranging the SHMM waveguide arrays along the x-direction with the transmission-phase distributions following Equation (5), a focusing lens (**Figure 5**a) can be designed without polarization-dependence. In the design, the focusing length, f, is set to be 250 mm, corresponding to numerical aperture (NA)

of 0.61, and φ_{0f} is assumed to be π for the purpose of getting an optimal focusing effect (See Note 10, Supporting Information, for the optimization of φ_{0f}). Here we have chosen to vary the width (Figure 5b,c) of the individual SHMM waveguide to provide the transmission-phase distributions required by Equation (5). It is observed from the near-field intensity distributions in Figure 5d–k that, the EM energy gradually converges to a focal plane both for x- and y-polarizations, and the experimental results are basically consistent with the simulation results. The estimated focusing lengths both for x- and y-polarizations are very close to the designed value of 250 mm. It can be inferred from the simulation and the measurement that the focusing spot size, defined as the full width at half maximum (FWHM) of the intensity distributions at the focal plane, is comparable to half of wavelength.

As has been discussed in the above section, the RHMM waveguide array can be designed to work as a half-wave plate. Further arrangement of the RHMM waveguide arrays with successive rotation angle can provide arbitrary phase distributions at the interface, hence enables reconstructing wavefront for CP EM waves. A fabricated RHMM waveguide array for beam deflection of the CP EM waves is shown in **Figure 6**a. The optimization of the geometrical parameters of the RHMM waveguide array as a half-wave plate is presented in detail in Note 11, Supporting Information. By adopting nine RHMM waveguides in a super cell and continuously rotating them with a constant step of $\pi/9$, the phase shifts satisfy the condition for beam deflecting by
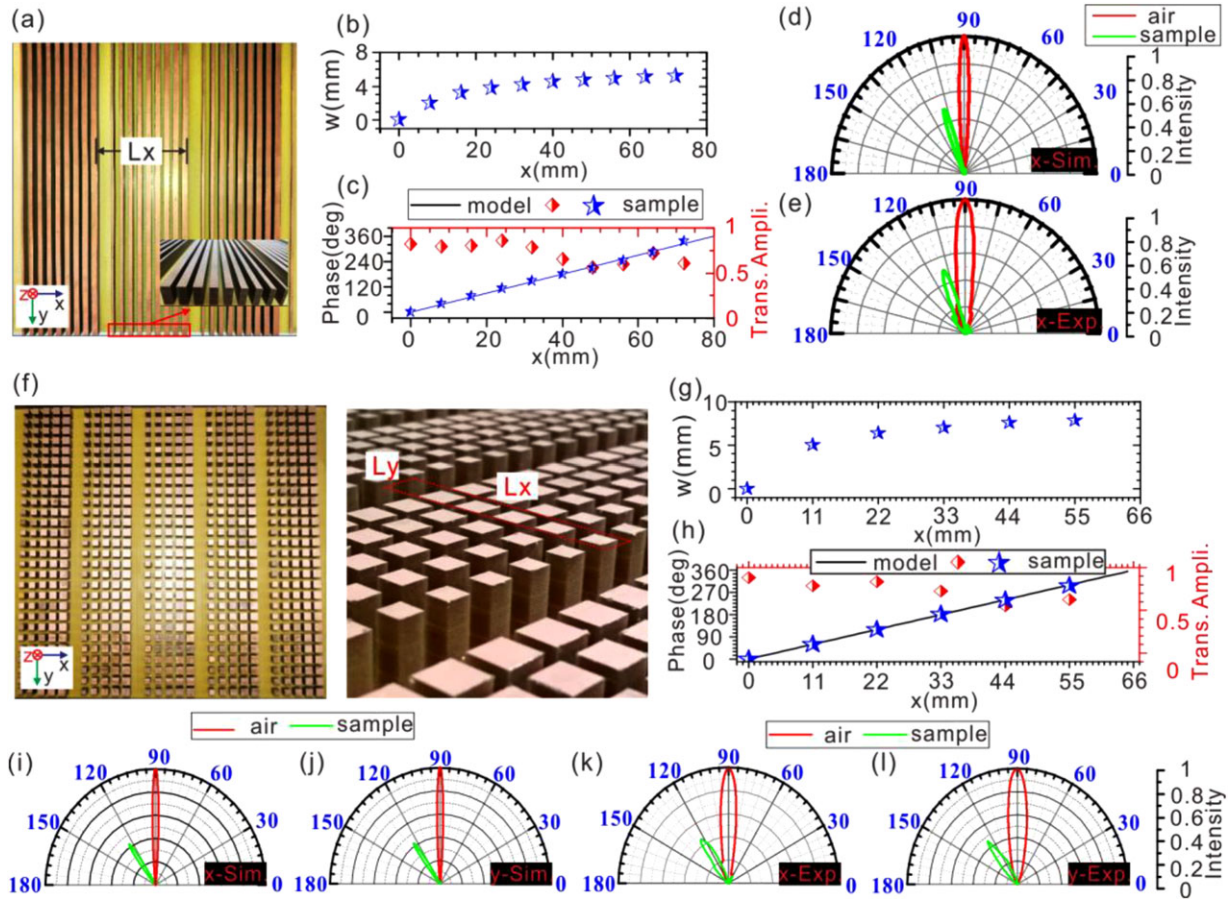
Figure 4. Beam deflectors for linearly polarized EM waves. a) The fabricated sample of the 1D-HMM waveguide array with an area of 248 mm × 300 mm and a height of 11.5 mm. b) The designed width, W, of each subunit within a super cell. c) The distributions of the transmission amplitude and phase shift of each subunit within a super cell at 12 GHz. The solid line is retrieved by Equation (4). The d) simulated and e) measured far-field electric field intensity for x-polarized incidence. The lattice constants of a super cell along the x-direction are $L_x = 10P = 80$ mm. f) The fabricated sample of the SHMM waveguide array with an area of 330 mm × 308 mm, and height of 16.4 mm. g) The designed width, W, of each subunit within a super cell. h) The distributions of the transmission amplitude and the phase shift of each subunit within a super cell at 8 GHz. The solid line is extracted from Equation (4). The i,j) simulated and k,l) measured (far-field electric field intensity for i,k) x-, and j,l) y-polarized incidences, respectively. The lattice constants along the x- and y-directions are $L_x = 6P = 66$ mm and $L_y (= P)$.

providing full 0–2π range and having a linear phase-gradient (Figure 6b). Meanwhile, the transmission intensity is kept highly uniform (Figure 6c). We can easily identify from the far-field intensity distributions (Figure 6d–g) that the transmitted EM waves are refracted along the designed anomalous angle as 19.7°. The transmitted EM waves with the RCP and LCP incidences, respectively, are refracted along left and right sides with respect to y-z plane due to the opposite sign of their phase gradients shown in Figure 6b. The simulated and measured near-field electric field distributions both for the RCP and LCP incidences can be found in Note 12, Supporting Information.

By successively rotating the RHMM waveguides to make the phase shifts to comply with Equation (5), a CP EM focusing lens with NA of 0.55 can be designed and fabricated (**Figure 7**a). The required phase profile along the interface with RCP incidence is depicted in Figure 7b. The simulated and measured results clearly indicate the focusing effect and a significantly enhanced field intensity (Figure 7c,e), when normally incident RCP EM waves illuminate the sample. The simulated focal length

of 220 mm, associated with the measured value of 234 mm, is smaller than the designed value of 260 mm due to finite-size effect.[50] Analogous to the previous dual-polarity metalens,[9] the focusing properties is altered between a convex lens and a concave lens by controlling the helicity of the incident beam. As a result, the CP EM lens exhibits a diverging effect when the LCP incident waves are used (See Note 13, Supporting Information, for the details).

2.3. Discussion

It is important to discuss the factors that affect the device performance in terms of conversion efficiency and diffraction efficiency for anomalous refracted beam. The modal characteristics of the SSP mode for an HMM waveguide array is highly dependent on the structural parameters. Actually, the five fabricated samples are more or less different from the predesigned structures. The
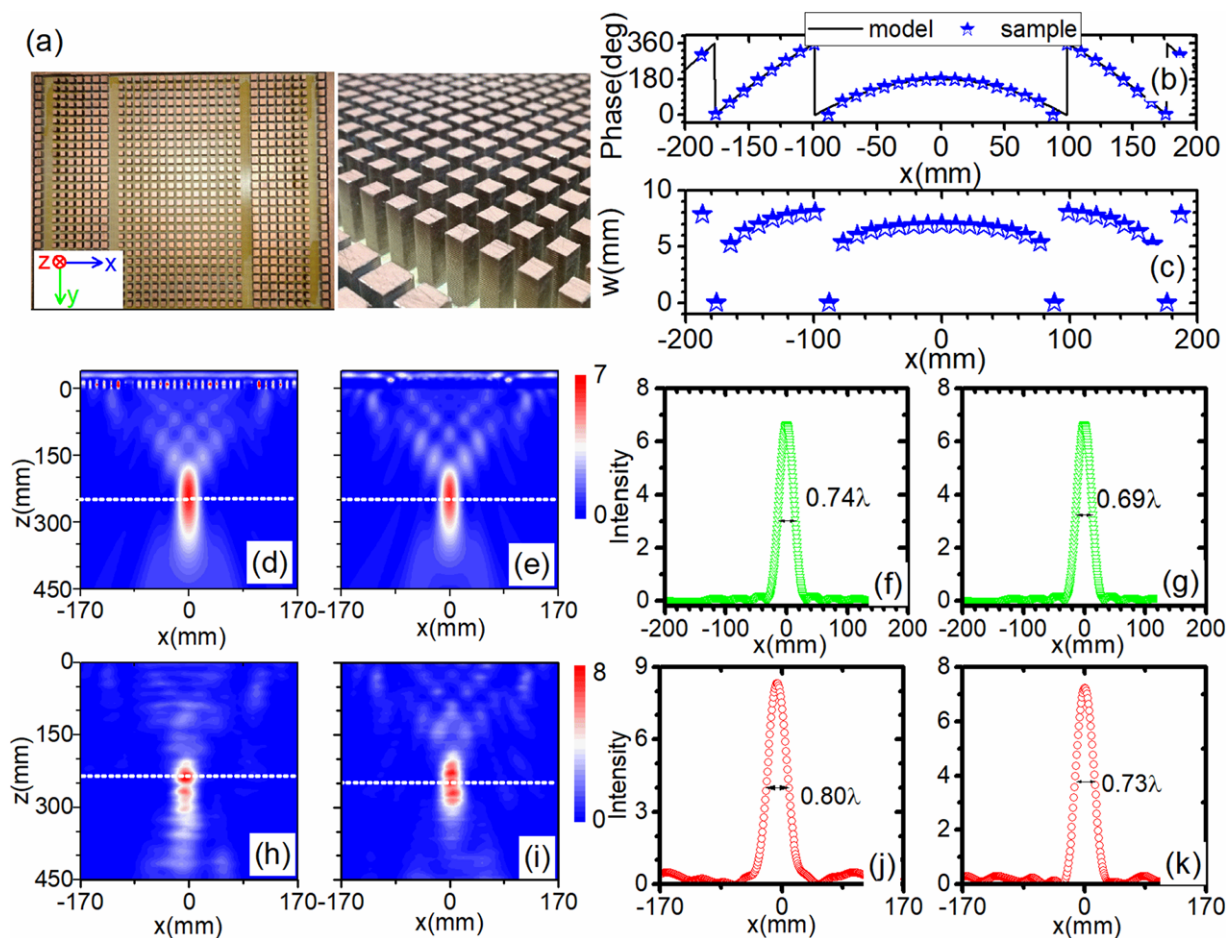
Figure 5. Focusing lens for linearly polarized EM waves. a) The fabricated sample of SHMM focusing lens with an area of 385 mm × 308 mm and a height of 16.4 mm. The distributions of the b) designed phase shift and c) waveguide width of each subunit at 8 GHz. The d,e) simulated and h,i) measured electric field intensity distributions in *x-z* plane with d,h) *x*-polarized, and e,i) *y*-polarized incidences, respectively. The f,g) simulated and j,k) experimental intensity profiles along the white dotted lines marked in (d),(e), and (h),(i), respectively. All the other parameters are the same as those in Figure 2.

fabricated HMM waveguide inevitably has to be slightly tapered, that is, the bottom width is a little larger than the top width. However, such a tapered HMM waveguide array incurs higher propagation loss compared to the designed structure without taper, resulting in a relatively lower conversion efficiency and diffraction efficiency. For example, the fabricated SHMM waveguide (Figure 4f) is linearly tapered with the bottom width 0.3 mm wider than the designed one. As a consequence, the practical diffraction efficiency and conversion efficiency are reduced to be approximately 79.4%, 42.9% for *x*-polarized incidence, and 95.8%, 40.2% for *y*-polarized incidence, where the conversion efficiencies are higher than that for a single plasmonic metasurface with a theoretical limit of 25%. These values are very close to the simulation values by taking account into the taper in the simulations. It is also worth emphasizing here, to cover the full 2π phase for beam deflecting, a HMM waveguide with a large width, associated with a high effective refractive index, is used, which will introduce significant mismatch between the propagation constant of the HMM waveguide array and the wave number in air (see Note 5, Supporting Information, for more details). In addition,

to design a practical HMM waveguide array for beam deflecting, a FR4 substrate is used, which will slightly enhance the reflection at the HMM–air interface as well. As a result, the transmission efficiency can be reduced for different HMM waveguides, especially for the one with a large width (see Note 8, Supporting Information, for the dependence of transmission on the width of HMM waveguide with the involvement of 2 mm FR4 substrate). Therefore, the transmission efficiency for an HMM waveguide array is highly suppressed since a significant portion of EM waves will be reflected back into the air at the incidence plane. The simulation results demonstrate that 42% for *x*-polarization (41.3% for *y*-polarization) and 35.2% for circular polarization of incident EM waves are, respectively, reflected back into the air for the SHMM (Figure 4) and RHMM (Figure 6) waveguide arrays for beam deflection, while merely 3% for *x*-polarization (1.6% for *y*-polarization) and 5.8% for circular polarization of incident EM waves are absorbed by the HMM waveguide arrays accordingly. We believe, provided the coupling issue solved, the resultant conversion efficiency can be significantly enhanced, being comparable to that with dielectric metasurfaces.[23,27,28,51] A promising
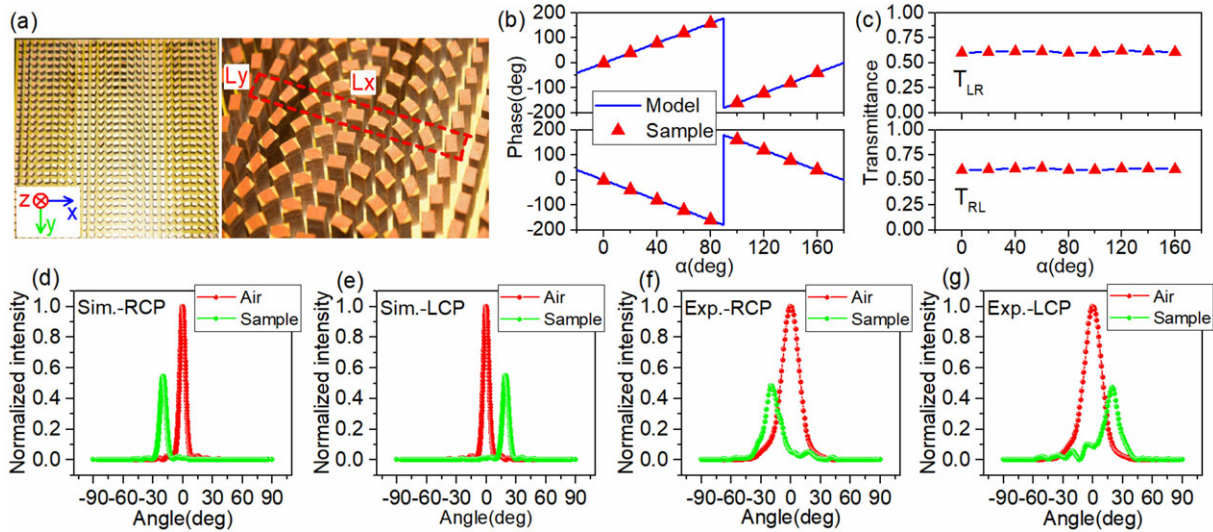
**ADVANCED
SCIENCE NEWS**

www.advancedsciencenews.com

LASER
&PHOTONICS
REVIEWS

www.lpr-journal.org

Figure 6. Beam deflectors for circularly polarized EM waves. a) The fabricated sample of the RHMM waveguide array with an area of 351 mm × 351 mm, and a height of 18.8 mm. A super cell comprised of nine RHMM waveguides with rotation angle step of $\pi/9$ ($L_x = 9P = 117$ mm, $L_y = P = 13$ mm). The cross-polarized phase shift and transmittance under normal incidence of RCP (upper side of (b), and upper side of (c)), and LCP (down side of (b), and down side of (c)), respectively. In the simulation, the operation frequencies in (b) and (c) are chosen as 7.6 GHz. The d,e) simulated and f,g) measured far-field electric field intensity profiles for d,f) RCP and e,g) LCP incidences at 7.6 GHz. All the other structural parameters are the same as those in Figure 2.
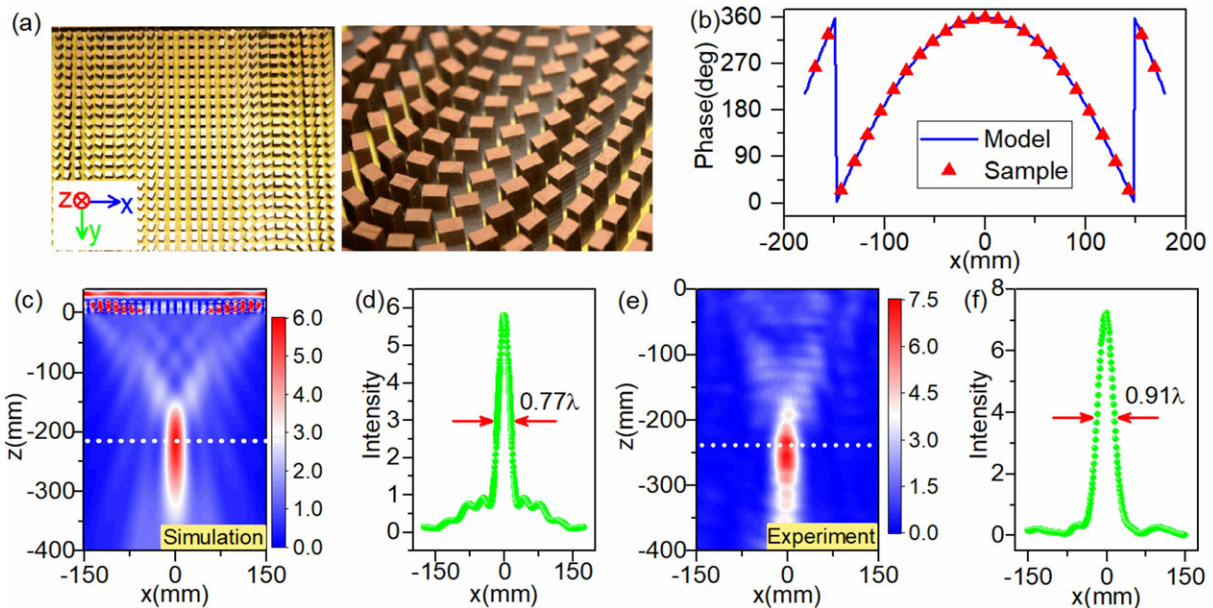

Figure 7. Focusing lens for circularly polarized EM waves. a) The fabricated sample of the RHMM focusing lens with an area of 351 mm × 286 mm, and a height of 18.8 mm. b) The designed phase distributions for RCP incidence at 7.6 GHz. The c) simulated and e) experimental electric field intensity distributions in x-z plane. The d) simulated and f) experimental intensity profiles along the white dotted lines denoted in (c) and (e), respectively. All the other parameters are the same as those in Figure 2.

approach to address the coupling issue is to add a tapered HMM waveguide array to overcome the momentum mismatch at the incidence plane, which has been exploited for ultra-wideband absorption with HMM waveguide arrays.[34,48,49] We are currently exploring some of these avenues.

Although we only show the device performance at one single frequency for each case in the main text, the operation band-width of the desired performance (>80% diffraction efficiency for beam deflecting) reaches a few tenths of 1 GHz (see Note 14, Supporting Information) and can be effectively enlarged if phase dispersion cancellation technique is used.[52] Besides, the HMM devices show rather robustness to the incidence angle since they can maintain a high level of diffraction/conversion efficiency even if the incidence angle greatly shifts to 20° (see

Note 15, Supporting Information, for more details). We also emphasize that the proposal could be extended to visible, infrared, and terahertz frequencies by scaling down the multilayer structure. We have shown in Note 16, Supporting Information, that the SSP modes can be supported with an HMM waveguide even in the near-infrared frequency region and the dispersion curve presents strong resemblance with that of the plasmonic mode in a metal waveguide of finite width. We note that the HMM waveguide takes advantage over this traditional plasmonic waveguide by pulling the dispersion relation further away from the light line, indicating the method of using the HMM waveguide array for control of EM waves is rather robust and flexible. The HMM metasurfaces have been further exploited to demonstrate anomalous refraction and focusing effect at 1550 nm (Notes 17–20, Supporting Information). We found the designed HMM metasurfaces made of silica of low refractive index of 1.45 can raise the conversion efficiency to 77.9% for the anomalous refracted beam, due to the significantly suppressed reflection at the HMM–air interface, while a low device thickness of only about a half wavelength is used. We believe that it is of great value to experimentally realize the HMM meta-devices at high frequencies, since the conversion efficiencies are comparable to those dielectric metasurfaces,[44,51,53] while our scheme requires neither high-index materials. In the optical region, the patterned multilayered structure can be fabricated by using deposition technique, such as electron beam evaporation, to precisely grow metal–dielectric multilayer, followed by focused-ion-beam etching to form the 2D array[31,54–57] (see Note 21, Supporting Information, for more details). We have considered the fabrication tolerance introduced by the experimental fabrication of the SHMM waveguide array, which shows that the influence of the thickness error (from deposition technique) on the diffraction/conversion efficiency can be neglected (please see Note 22, Supporting Information, for more details). The tapered sidewall profiles of the SHMM waveguides, originating from etching technique, can slightly deteriorate the device performances, but the diffraction/conversion efficiency can still reach as high as 93% (60%), and 96% (57%) for x- and y-polarized incidences, even if the slant angle is assumed to be 5°, slightly larger than that used in the metamaterials with Ag/MgF_2 multilayered pattern in the near-infrared domain[54] (please see Note 23, Supporting Information, for more details).

3. Conclusions

We have demonstrated that an HMM waveguide composed of alternating metal–dielectric multilayers of finite width surrounded with air can always support the SSP modes at both sides of HMM–air interfaces, which have strongly similar properties with the plasmonic mode of a metal surface. The dispersion relation of the SSP mode can be engineered at will by tuning the geometrical parameters defining the HMM. A new metasurface platform based on the HMM waveguide array allows the full control of phase delay of the incident EM waves, which enables us to reshape the wavefront of the transmitted EM waves in nearly arbitrary ways. A novel kind of beam deflector and focusing lens with the HMM waveguides have been designed, fabricated and measured, demonstrating highly efficient anomalous refraction and diffraction-limited focusing both for linear and circular

polarizations. The designed, simulated, and measured results of the anomalous refraction angle are all in very good agreement. Besides, the measured maximum conversion efficiency for anomalous refracted beam is 42.9% and can be highly expected to be significantly enhanced if high-efficiency coupling mechanism is introduced. Our results can lead to a variety of applications, such as polarization and spectral beam splitters, beam deflectors, flat lenses, phase modulators, and so forth. We expect the presented results could advance a new class of research on EM functional devices based on the HMM metasurfaces, particularly at high frequencies, with the existing fabrication technology.

Supporting Information

Supporting Information is available from the Wiley Online Library or from the author.

Acknowledgements

Conflict of Interest

The authors declare no conflict of interest.

Keywords

[1] J. Hao, Y. Yuan, L. Ran, T. Jiang, J. A. Kong, C. T. Chan, L. Zhou, *Phys. Rev. Lett.* **2007**, *99*, 063908.

[2] N. I. Landy, S. Sajuyigbe, J. J. Mock, D. R. Smith, W. J. Padilla, *Phys. Rev. Lett.* **2008**, *100*, 207402.

[3] A. Melikyan, L. Alloatti, A. Muslija, D. Hillerkuss, P. C. Schindler, J. Li, R. Palmer, D. Korn, S. Muehlbrandt, D. Van Thourhout, B. Chen, R. Dinu, M. Sommer, C. Koos, M. Kohl, W. Freude, J. Leuthold, *Nat. Photonics* **2014**, *8*, 229.

[4] R. A. Shelby, D. R. Smith, S. Schultz, *Science* **2001**, *292*, 77.

[5] Z. Liu, H. Lee, Y. Xiong, C. Sun, X. Zhang, *Science* **2007**, *315*, 1686.

[6] X. Ni, Z. J. Wong, M. Mrejen, Y. Wang, X. Zhang, *Science* **2015**, *349*, 1310.

[7] N. Yu, P. Genevet, M. A. Kats, F. Aieta, J.-P. Tetienne, F. Capasso, Z. Gaburro, *Science* **2011**, *334*, 333.

[8] S. Sun, Q. He, S. Xiao, Q. Xu, X. Li, L. Zhou, *Nat. Mater.* **2012**, *11*, 426.

[9] X. Chen, L. Huang, H. Mühlenbernd, G. Li, B. Bai, Q. Tan, G. Jin, C.-W. Qiu, S. Zhang, T. Zentgraf, *Nat. Commun.* **2012**, *3*, 1198.

[10] N. Yu, F. Capasso, *Nat. Mater.* **2014**, *13*, 139.

[11] D. Lin, P. Fan, E. Hasman, M. L. Brongersma, *Science* **2014**, *345*, 298.

[12] N. Meinzer, W. L. Barnes, I. R. Hooper, *Nat. Photonics* **2014**, *8*, 889.

[13] F. Aieta, M. A. Kats, P. Genevet, F. Capasso, *Science* **2015**, *347*, 1342.

[14] W. Sun, Q. He, S. Sun, L. Zhou, *Light: Sci. Appl.* **2016**, *5*, e16003.

[15] Y. Yang, L. Jing, B. Zheng, R. Hao, W. Yin, E. Li, C. M. Soukoulis, H. Chen, *Adv. Mater.* **2016**, *28*, 6866.

[16] X. Ni, S. Ishii, A. V. Kildishev, V. M. Shalaev, *Light: Sci. Appl.* **2013**, *2*, e72.

[17] L. Huang, X. Chen, H. Mühlenbernd, H. Zhang, S. Chen, B. Bai, Q. Tan, G. Jin, K.-W. Cheah, C.-W. Qiu, J. Li, T. Zentgraf, S. Zhang, *Nat. Commun.* **2013**, *4*, 2808.

[18] G. Zheng, H. Mühlenbernd, M. Kenney, G. Li, T. Zentgraf, S. Zhang, *Nat. Nanotechnol.* **2015**, *10*, 308.

[19] M. I. Shalaev, J. Sun, A. Tsukernik, A. Pandey, K. Nikolskiy, N. M. Litchinitser, *Nano Lett.* **2015**, *15*, 6261.

[20] F. Monticone, N. M. Estakhri, A. Alù, *Phys. Rev. Lett.* **2013**, *110*, 203903.

[21] C. Pfeiffer, A. Grbic, *Phys. Rev. Lett.* **2013**, *110*, 197401.

[22] C. Pfeiffer, N. K. Emani, A. M. Shaltout, A. Boltasseva, V. M. Shalaev, A. Grbic, *Nano Lett.* **2014**, *14*, 2491.

[23] M. Decker, I. Staude, M. Falkner, J. Dominguez, D. N. Neshev, I. Brener, T. Pertsch, Y. S. Kivshar, *Adv. Opt. Mater.* **2015**, *3*, 813.

[24] H. Zuo, D.-Y. Choi, X. Gai, P. Ma, L. Xu, D. N. Neshev, B. Zhang, B. Luther-Davies, *Adv. Opt. Mater.* **2017**, *5*, 1700585.

[25] B. H. Chen, P. C. Wu, V.-C. Su, Y.-C. Lai, C. H. Chu, I. C. Lee, J.-W. Chen, Y. H. Chen, Y.-C. Lan, C.-H. Kuan, *Nano Lett.* **2017**, *17*, 6345.

[26] S. Wang, P. C. Wu, V.-C. Su, Y.-C. Lai, M.-K. Chen, H. Y. Kuo, B. H. Chen, Y. H. Chen, T.-T. Huang, J.-H. Wang, *Nat. Nanotechnol.* **2018**, *13*, 227.

[27] M. Khorasaninejad, W. T. Chen, R. C. Devlin, J. Oh, A. Y. Zhu, F. Capasso, *Science* **2016**, *352*, 1190.

[28] M. Khorasaninejad, W. T. Chen, A. Y. Zhu, J. Oh, R. C. Devlin, D. Rousso, F. Capasso, *Nano Lett.* **2016**, *16*, 4595.

[29] J. T. Shen, P. B. Catrysse, S. Fan, *Phys. Rev. Lett.* **2005**, *94*, 197401.

[30] X. Yang, J. Yao, J. Rho, X. Yin, X. Zhang, *Nat. Photonics* **2012**, *6*, 450.

[31] D. Lu, J. J. Kan, E. E. Fullerton, Z. Liu, *Nat. Nanotechnol.* **2014**, *9*, 48.

[32] C. Argyropoulos, N. M. Estakhri, F. Monticone, A. Alù, *Opt. Express* **2013**, *21*, 15037.

[33] Z. Jacob, L. V. Alekseyev, E. Narimanov, *Opt. Express* **2006**, *14*, 8247.

[34] Y. Cui, K. H. Fung, J. Xu, H. Ma, Y. Jin, S. He, N. X. Fang, *Nano Lett.* **2012**, *12*, 1443.

[35] T. Galfsky, J. Gu, E. E. Narimanov, V. M. Menon, *Proc. Natl. Acad. Sci.* **2017**, *114*, 5125.

[36] T. Galfsky, Z. Sun, C. R. Considine, C.-T. Chou, W.-C. Ko, Y.-H. Lee, E. E. Narimanov, V. M. Menon, *Nano Lett.* **2016**, *16*, 4940.

[37] E. E. Narimanov, *Phys. Rev. X* **2014**, *4*, 041014.

[38] D. R. Smith, J. B. Pendry, M. C. K. Wiltshire, *Science* **2004**, *305*, 788.

[39] F. J. Garcia-Vidal, L. Martín-Moreno, J. B. Pendry, *J. Opt. A: Pure Appl. Opt.* **2005**, *7*, S97.

[40] S. A. Maier, S. R. Andrews, L. Martín-Moreno, F. J. García-Vidal, *Phys. Rev. Lett.* **2006**, *97*, 176805.

[41] C. R. Williams, S. R. Andrews, S. A. Maier, A. I. Fernández-Domínguez, L. Martín-Moreno, F. J. García-Vidal, *Nat. Photonics* **2008**, *2*, 175.

[42] X. Shen, T. J. Cui, D. Martin-Cano, F. J. Garcia-Vidal, *Proc. Natl. Acad. Sci.* **2013**, *110*, 40.

[43] J. Yang, J. Wang, M. Feng, Y. Li, X. Wang, X. Zhou, T. Cui, S. Qu, *Appl. Phys. Lett.* **2017**, *110*, 203507.

[44] M. Khorasaninejad, F. Capasso, *Nano Lett.* **2015**, *15*, 6709.

[45] N. M. Estakhri, A. Alù, *Phys. Rev. X* **2016**, *6*, 041008.

[46] The Bloch mode calculations were carried out with Bandsolve software from Rsoft Design Group, http://www.rsoftdesign.com (accessed: 2013)

[47] A. W. Snyder, J. D. Love, *Optical Waveguide Theory*, Kluwer, London **1983**.

[48] H. Hu, D. Ji, X. Zeng, K. Liu, Q. Gan, *Sci. Rep.* **2013**, *3*, 1249.

[49] X. Yin, L. Chen, X. Li, *J. Lightwave Technol.* **2015**, *33*, 3704.

[50] L. Verslegers, P. B. Catrysse, Z. Yu, J. S. White, E. S. Barnard, M. L. Brongersma, S. Fan, *Nano Lett.* **2009**, *9*, 235.

[51] M. Khorasaninejad, K. B. Crozier, *Nat. Commun.* **2014**, *5*, 5386.

[52] L. Chen, X. Ke, H. Guo, J. Li, X. Li, L. Zhou, *Sci. Rep.* **2018**, *8*, 1051.

[53] P. R. West, J. L. Stewart, A. V. Kildishev, V. M. Shalaev, V. V. Shkunov, F. Strohkendl, Y. A. Zakharenkov, R. K. Dodds, R. Byren, *Opt. Express* **2014**, *22*, 26212.

[54] J. Valentine, S. Zhang, T. Zentgraf, E. Ulin-Avila, D. A. Genov, G. Bartal, X. Zhang, *Nature* **2008**, *455*, 376.

[55] S. S. Kruk, Z. J. Wong, E. Pshenay-Severin, K. O'Brien, D. N. Neshev, Y. S. Kivshar, X. Zhang, *Nat. Commun.* **2016**, *7*, 11329.

[56] D. Ji, H. Song, X. Zeng, H. Hu, K. Liu, N. Zhang, Q. Gan, *Sci. Rep.* **2015**, *4*, 4498.

[57] D. Lu, H. Qian, K. Wang, H. Shen, F. Wei, Y. Jiang, E. E. Fullerton, P. K. L. Yu, Z. Liu, *Adv. Mater.* **2018**, *30*, 1706411.